ENGINEERING MICROSTRUCTURES OF SLAG-BLENDED CEMENTS AND ALKALI-ACTIVATED FOAMS - EXPERIMENTS AND MODELLING

Vít ŠMILAUER[1], Michal HLOBIL[1], Petr HLAVÁČEK[1,2]

[1] Department of Mechanics, Faculty of Civil Engineering, Czech Technical University in Prague, Thákurova 7, 166 29 Prague 6, Czech Republic

[2] Bundesanstalt für Materialforschung und -prüfung (BAM), Unter den Eichen 87, 122 05 Berlin, Germany

vit.smilauer@fsv.cvut.cz, michal.hlobil@fsv.cvut.cz, petr.hlavacek@fsv.cvut.cz

Introduction

Engineered microstructures play important role in material improvement and optimisation covering alloys, semiconductors, biomaterials, ceramics, or construction materials. Since 1980's, microstructure engineering *via* multiscale modelling became popular due to available computer power for solving large systems of equations and more predictive material models[1].

Focusing solely on cementitious materials, strength, as the most important property, has been linked to gel/space ratio as already recognised by Powers and Brownyard[2] for various w/b ratios and maturity. Since gel is mostly composed of C-S-H in OPC-based systems, C-S-H/space descriptor provides good phenomenological law as well[3]. This statement was verified by fitting power law to the results from an open database CemBase[4], see Figure 1. The figure contains 63 points for OPC, 5 for slag blends at 43% OPC replacement level, 5 for 35% fly ash blends, 6 for pure C_3S, and 6 for pure C_2S.

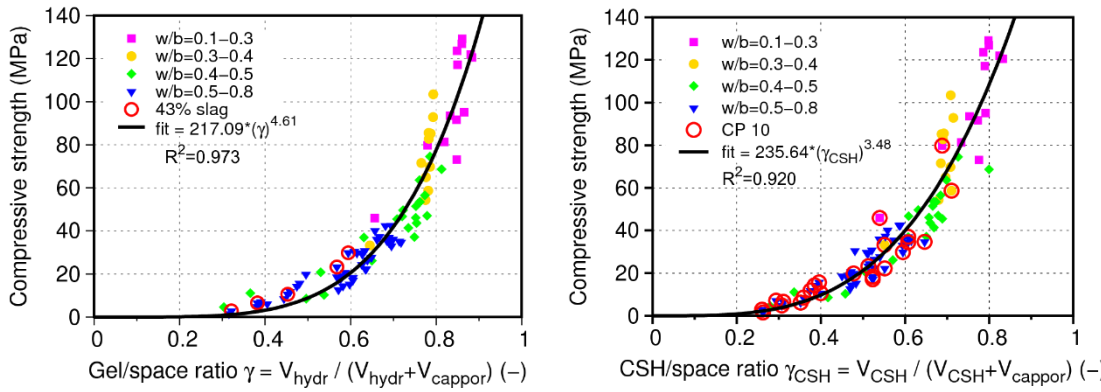

Figure 1: Compressive strength as function of gel/space and C-S-H/space ratios on OPC and blended cement pastes. Slag cements are marked by circles

Multiscale modelling of concrete can be traced down to Roelfstra *et al.*[5], who considered mesoscale concrete structure with crack propagation. Bernard *et al.*[6] presented an analytical multiscale model for cement paste, mortar and concrete

elasticity which was later extended for strength predictions by Pichler and Hellmich[7]. 2D and 3D lattice models for concrete strength exists[8,9], to mention a few. A four-scale continuum-based model for cement paste strength was elaborated by Hlobil *et al.*[11], allowing to take into account spatial distribution of C-S-H phase, volume fractions of relevant phases on each scale and elastic-fracture properties of individual phases. Due to important consequences, this model is presented further in details.

Multiscale model for blended cement paste

Multiscale model for elasticity and strength predictions requires the formulation of constitutive material laws. The tensile strength at each level is identified from compressive strength f_c. Compressive strength is evaluated from a fracture material model, considering that every failing phase has internal defects in the shape of 2D ellipsoids as introduced by Griffith[10]. Under macroscopic compressive stress, a crack propagates from a critically-aligned ellipsoid into the matrix and an equivalent strain can be calculated as

$$\tilde{\varepsilon} = \frac{1}{E} \cdot \frac{-(\sigma_1 - \sigma_3)^2}{8(\sigma_1 + \sigma_3)} \tag{1}$$

where $\sigma_{1,3}$ are principal stresses in a material point[11]. The equivalent strain enters isotropic damage law, leading eventually to material softening. An interesting feature of the Griffith model is that the ratio of the uniaxial compressive-to-tensile strength equals to 8 as encountered often in concrete, regardless of aspect ratio of ellipsoids.

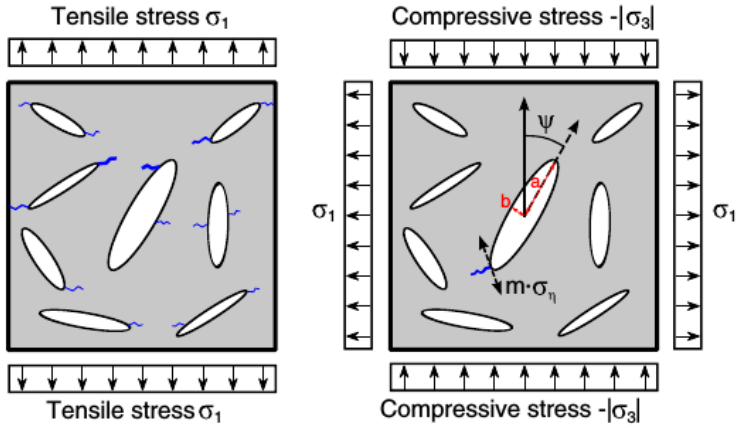

Figure 2: Crack evolution during uniaxial tensile stress (left) and during compressive loading (right)

The Griffith's model is extended with Rankine cut-off model, controlling maximum tensile stress in the matrix. The performance of the proposed Griffith-Rankine model under the plane stress condition is similar to Mohr-Coulomb model used for cohesive-frictional materials[11]. Isotropic damage mechanics is used for calculating damage extent.

The four-level hierarchical model is constructed according to Figure 3 with the particular levels as:

- **Level 0: C-S-H** considers C-S-H globules packed to densities between C-S-H_{LD} and C-S-H_{HD}. The globules become mixed with small and large gel pores (1 nm < d < 12 nm). The characteristic size spans the range of 1 - 100 nm.
- **Level 1: C-S-H foam** contains homogenised C-S-H together with capillary pores. To mimic an uneven distribution of C-S-H among clinker grains, C-S-H have a spatial gradient. The characteristic size spans the range of 100 nm-10 µm.
- **Level 2: Cement paste** adds unhydrated clinker and all remaining hydration products (CH, AFm, AFt, ...) inside the homogenised C-S-H foam. The characteristic size spans the range of 10 - 100 µm.
- **Level 3: Cement paste with air** captures entrained or entrapped air, decreasing the resulting mechanical properties. The characteristic size spans the range of 100-1000 µm.

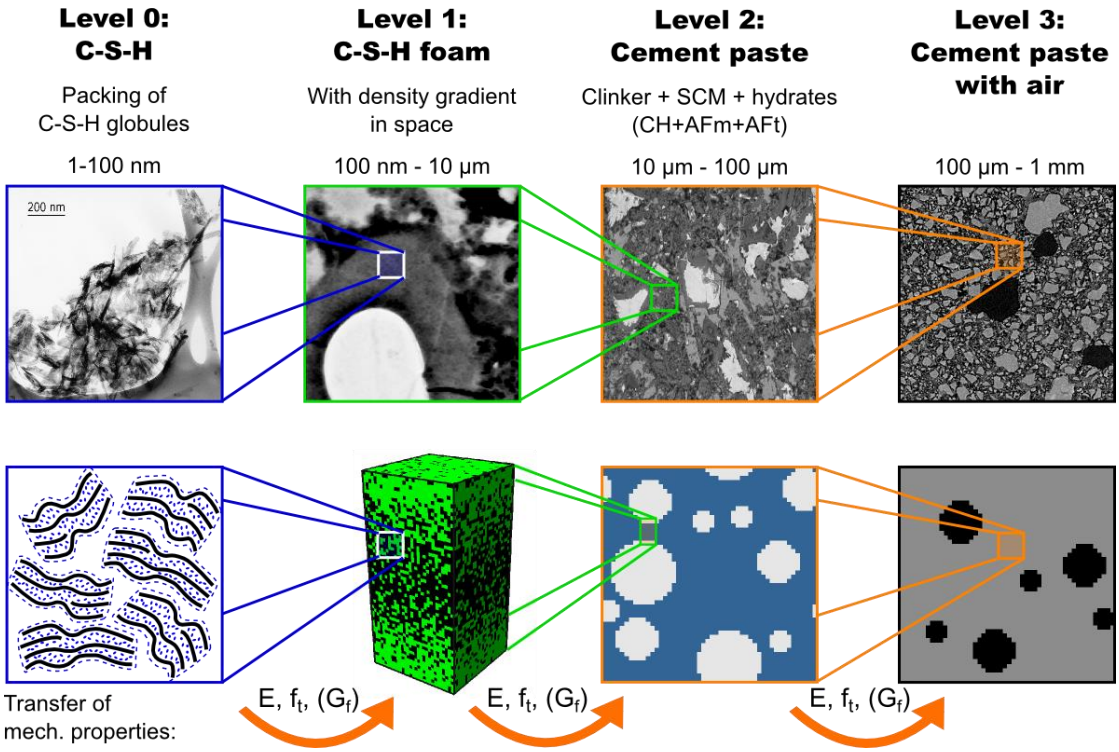

Figure 3: A four-level hierarchical multiscale model for blended cement pastes[11]

The coupling between levels occurs through upscaling the elastic modulus E, tensile strength f_t and fracture energy G_f. The fracture energy G_f is estimated from the underlying level in order to guarantee correct dissipation of energy. Intrinsic elastic-fracture properties of phases are summarised in Table 1.

Table 1: Intrinsic elastic and apparent fracture properties

Phase	Elastic modulus (GPa)	Poisson's ratio (-)	Tensile (compressive) strength (MPa)	Fracture energy (J/m^2)
C-S-H globule	57.1	0.27	320 (2560)	2
C-S-H_{LD} predicted	21.7	0.24	66 (528)	5
C-S-H_{HD} predicted	29.4	0.24	107 (856)	5
Water-filled porosity	0.001	0.499924	-	-
CH	38	0.305	-	-
AFt	22.4	0.25	-	-
AFm	42.3	0.324	-	-
Clinker minerals	139.9	0.30	-	-

Spatial distribution of C-S-H

C-S-H nucleating in the region between individual clinker grains result in a spatial gradient. This can be proved by calculating probability density from a nearest clinker grain surface by taking microtomography NIST data in Figure 4. The multiscale model implements the spatial distribution of C-S-H in the computational unit cell (UC) in Figure 5, which is composed from a 3D uniform mesh, consisting of 20 × 20 × 40 brick elements with linear displacement interpolations and with a resolution of 0.25 µm/voxel, yielding the UC size of 5 ×5 × 10 µm.

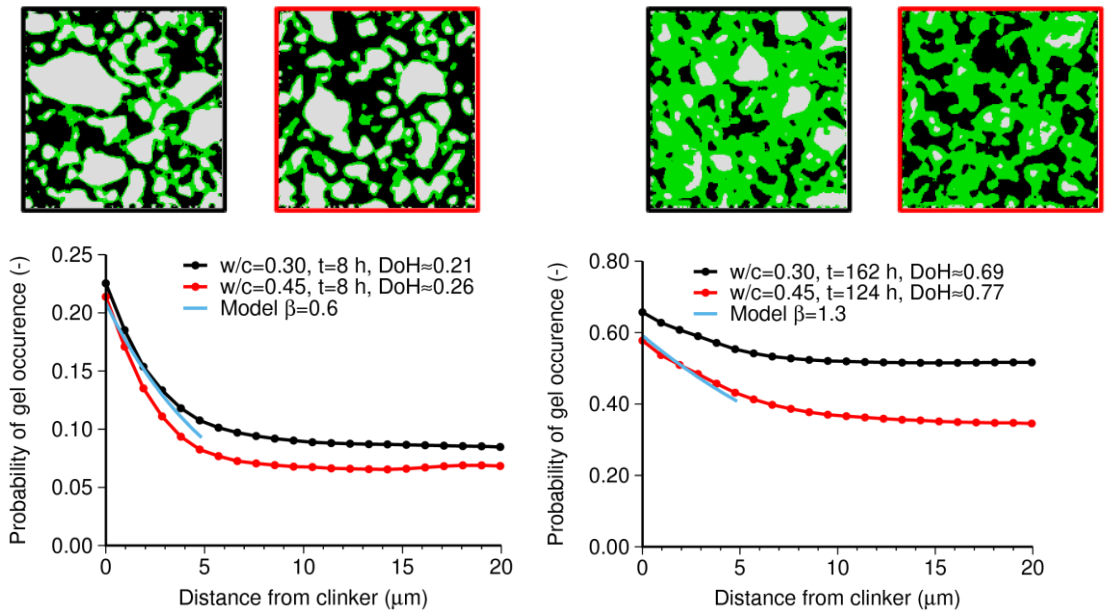

Figure 4: The impact of the parameter β on the C-S-H distribution (Level 1) for C-S-H/space ratio 0.7, UC size 5×5×10 µm

Exponential distribution approximates the spatial gradient in the microstructure as

$$\rho(x,\beta) = \frac{1}{\beta}\exp\left(\frac{-x/\ell_{UC}}{\beta}\right) \quad (2)$$

where *x* stands for the distance from the clinker grain surface, β is a parameter of the exponential distribution and ℓ_{UC} is the characteristic length of UC. Low values of β indicate a high gradient of C-S-H in space. The most probable value is β=0.6, covering w/b in the range 0.157 to 0.68, young and mature pastes.

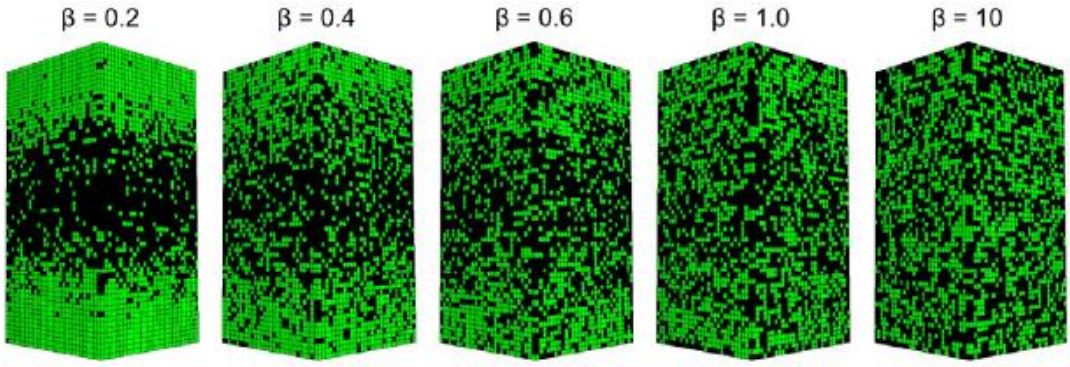

Figure 5: The impact of the parameter β on the C-S-H distribution (Level 1) for C-S-H/space ratio 0.7, UC size 5×5×10 μm

Strength validation for pastes

Performance of four-scale model is first validated on OPC with w/b=0.51. Volume fractions of phases were obtained from Lafarge Centre de Recherche using a combination of XRD/Rietveld/TGA and volume balance equations. The results in Figure 6 show excellent performance of the multiscale model.

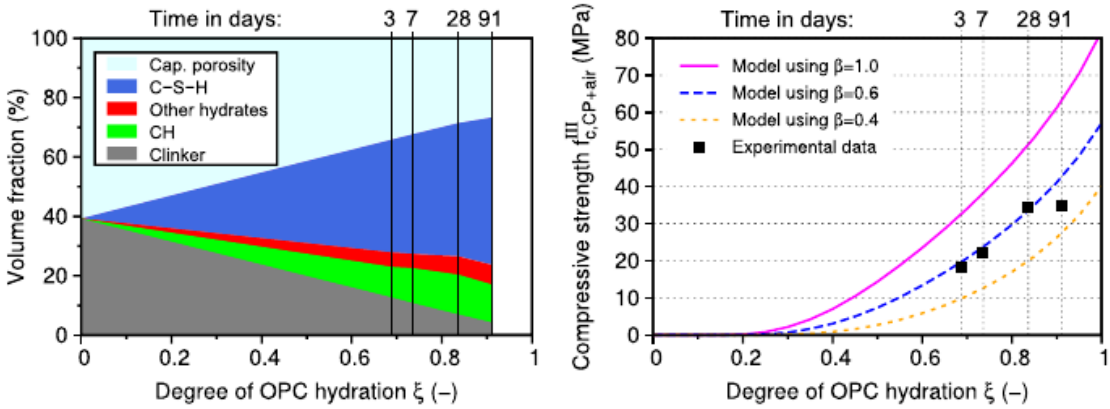

Figure 6: Volume fractions and strength for OPC paste with w/b=0.51

Figure 7 shows model performance for OPC w/b=0.247. Due to lower mutual distance of cement grains, spatial distribution of C-S-H plays less important role.

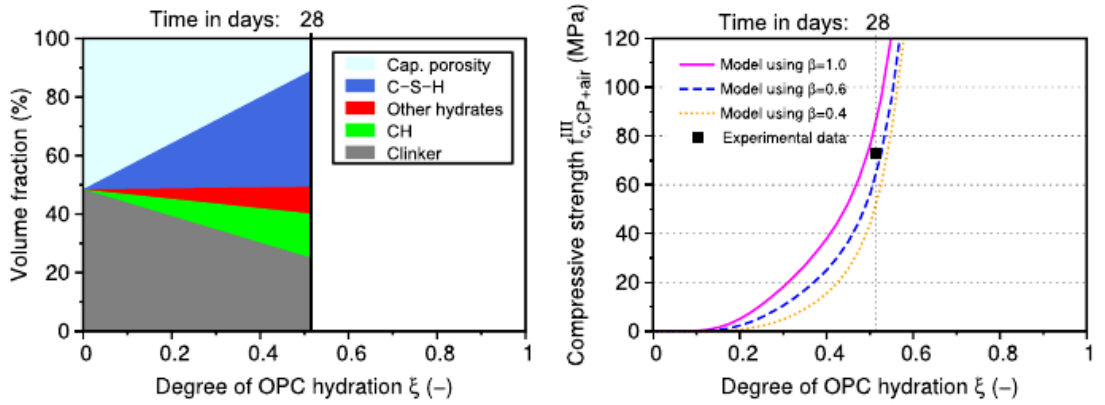

Figure 7: Volume fractions and strength for OPC paste with w/b=0.247

The results from a microstructural characterisation carried out on a slag-blended paste with w/b = 0.53 with slag replacement 43% are showed in Figure 8. Cement fineness 363 m^2/kg was comparable with a slag fineness of 350 m^2/kg. Model over-predictions after 7 days can be attributed to less tighter distribution of hydrates around slag particles or other effects uncaptured by model.

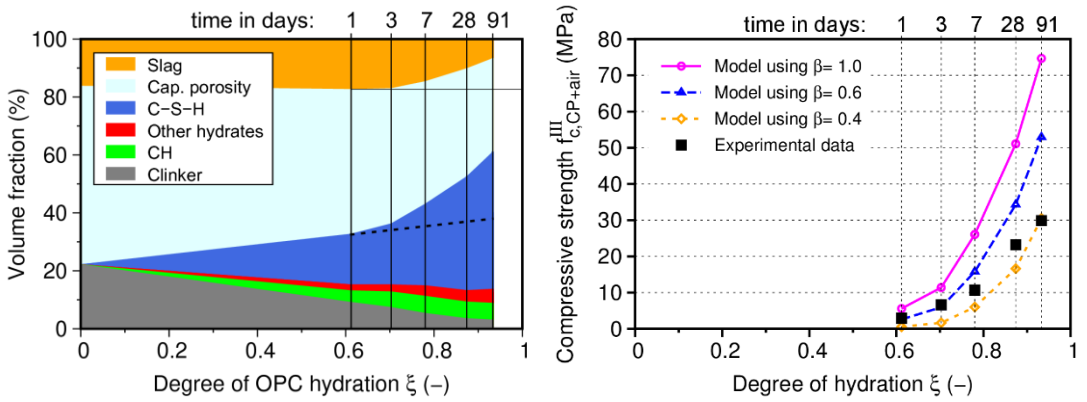

Figure 8: Volume fractions and strength for slag-blended paste with w/b=0.53

Figure 9 shows the overall validation for 95 measured compressive strengths of pastes, namely 76 OPC, 5 blended with slag, 5 blended with fly ash, 5 blended with limestone, and 4 blended with quartz. The data were gathered from different sources and entered into database CemBase[4].

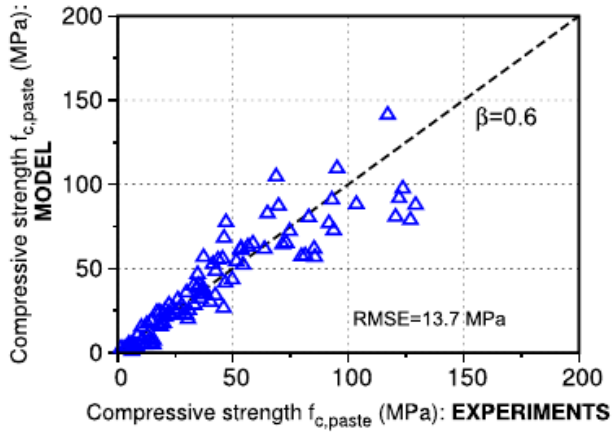

Figure 9: Validation of overall model-predicted compressive strength

Strength scaling

Although the multiscale model gives reasonable predictions for OPC and blended cements on the level of paste, cohesive properties of C-S-H seem to be underestimated with regards to experiments. Direct measurements on cantilever beam in inner product (mainly C-S-H_{HD}) showed cohesive strength 700.2 ± 198.5 MPa[17], see Figure 10, while the multiscale model predicts only 107 MPa obtained from a downscaling identification.

The multiscale simulations consider deterministic size effect stemming from energy release rate in fracture process zone. However, finite size of UC at each level may miss sufficiently large representation since crack initiation and propagation depends on weakest link in the microstructure. To shed further light on this phenomenon, levels I+II were merged together and tested for a statistical size effect.

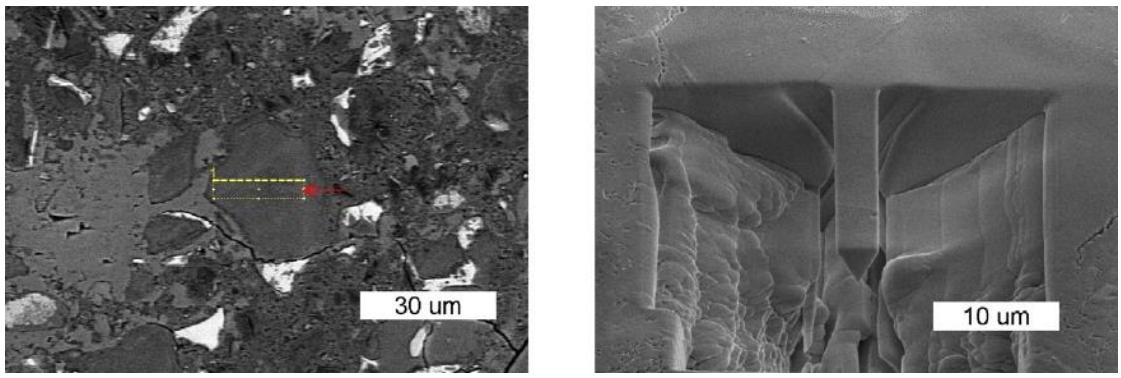

Figure 10: Direct bending of cantilever beams made from old cement paste, zone of inner product[17]

Microstructures combining levels I+II were generated from edge sizes 25 up to 200 µm, see Figure 11. They contain only three phases, *i.e.* clinker, C-S-H and capillary porosity and correspond to w/b=0.40 and degree of hydration 0.40. Statistical scaling of strength follows Weibull's theory of a weakest link reading

$$f_c = f_{c,0}\left(\frac{V}{V_0}\right)^{\frac{-1}{m}} \tag{3}$$

where V_0 is a reference volume for obtaining reference strength $f_{c,0}$. Since the formula is a power-law, the absolute value for V_0 becomes unimportant on scaling. Results in Figure 12 show Weibull's modulus m=7.23 which is comparable with m=7.91 used for concrete uniaxial tensile test[12]. In this regard, strength reduction between 25 and 1000 µm microstructures gives a factor of 0.600. Hence, the down-scaling must lead to a higher C-S-H cohesion then predicted by current multiscale model.

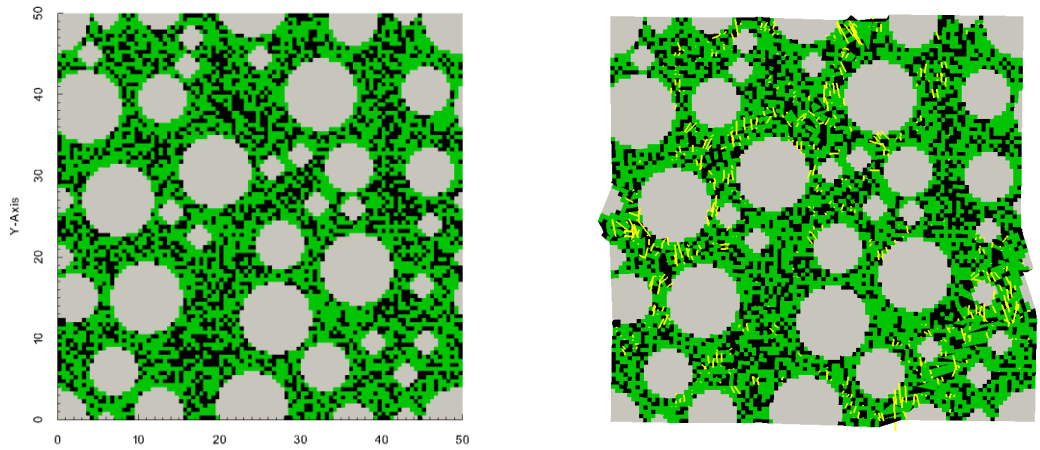

Figure 11: Microstructure combining Levels I+II, 50x50 µm, 0.5 µm/pixel, β=0.6. Unloaded microstructure (left) and at state of maximum compressive stress (right). Grey = cement grains, green = C-S-H, black = capillary porosity, yellow = cracks

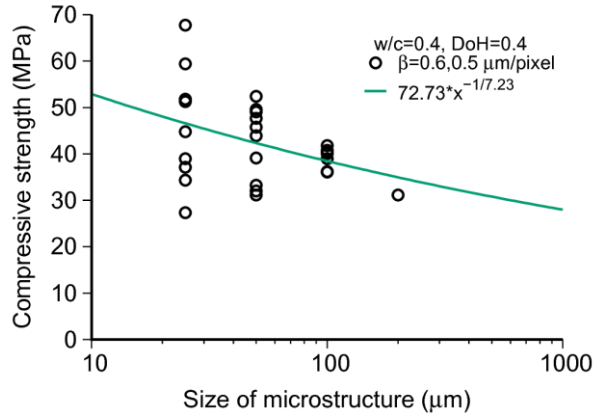

Figure 12: Scaling of compressive strength at Level I+II including statistical size effect

Alkali-activated fly ash foams

Alkali-activated materials have been in focus since Hans Kühl received the first patent in 1908 and Purdon described alkali-activation of slag in 1940. Intensive research was devoted to the process of polymerisation from different precursors, containing slag,

fly ash, clay-like materials, soils *etc.*[14]. Our previous research led to volumetric model of alkali-activated, low-calcium fly ash[15] and quantified three relevant phases, *i.e.* fly ash skeleton, solid N-A-S-H gel particles and open porosity, see Figure 13. Such paste provides compressive strength over 50 MPa and can be used further for concrete production, for example.

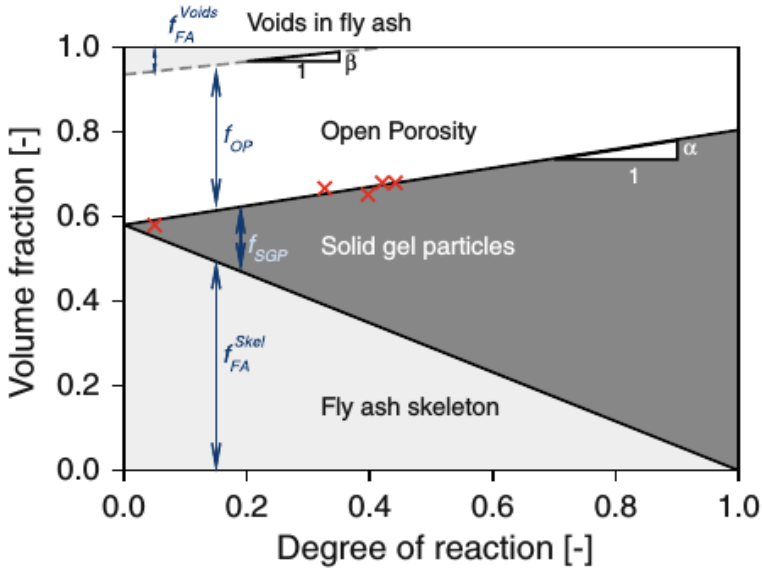

Figure 13: Calibrated model for alkali-activated fly ash

An alkali-activated fly ash foam can be prepared by aerating the fly ash paste with hydrogen using an aluminium powder[16]. Hydrogen liberation during the activation process leads to a closed-pore network. The fly ash class F from the Opatovice brown coal power plant, Czech Republic (Blaine 210 m^2/kg) is used as the source material for alkali-activation, see Table 2. The aluminium metal powder (Al) from Albo Schlenk Inc., Bojkovice, Czech Republic, product type 76013 (average particle diameter by mass, d50 ≈ 35 µm), is used as an air entraining agent.

Table 2: Composition of fly ash (wt%)

SiO_2	Al_2O_3	Fe_2O_3	CaO	K_2O	TiO_2
51.9	32.8	6.3	2.7	2.12	1.89

Sodium hydroxide pellets dissolved in standard sodium metasilicate constitute the alkali activator. The solid/liquid ratio and the amount of Al metal powder is optimised with respect to the foam stability, porosity, and pore distribution. The final compositions of the mixes are given in Table 3 and polished sections are in Figure 14. The foams are prepared by hand stirring and introducing a liquid activator to solid intermixed materials. The moulds are kept under laboratory conditions at 22°C for 2 h and subsequently cured in the oven for 12 h at 80°C.

Table 3: Compositions for alkali-activated fly-ash foams (the listed masses fill approximately the volume of 100 ml)

Mixture	Fly ash (g)	Liquid / solid (wt%)	NaOH (g)	Na metasilicate (g)	Al (g)	Bulk density (kg/m^3)
FAF1	50	0.37	2.8	15.7	0.03	751
FAF 2	50	0.38	2.9	16.1	0.03	778
FAF 3	50	0.39	3.0	16.5	0.03	772
FAF 4	50	0.37	2.8	15.7	0.045	700
FAF 5	50	0.38	2.9	16.1	0.045	671
FAF 6	50	0.39	3.0	16.5	0.045	626
FAF 7	50	0.37	2.8	15.7	0.06	574
FAF 8	50	0.38	2.9	16.1	0.06	521
FAF 9	50	0.39	3.0	16.5	0.06	422

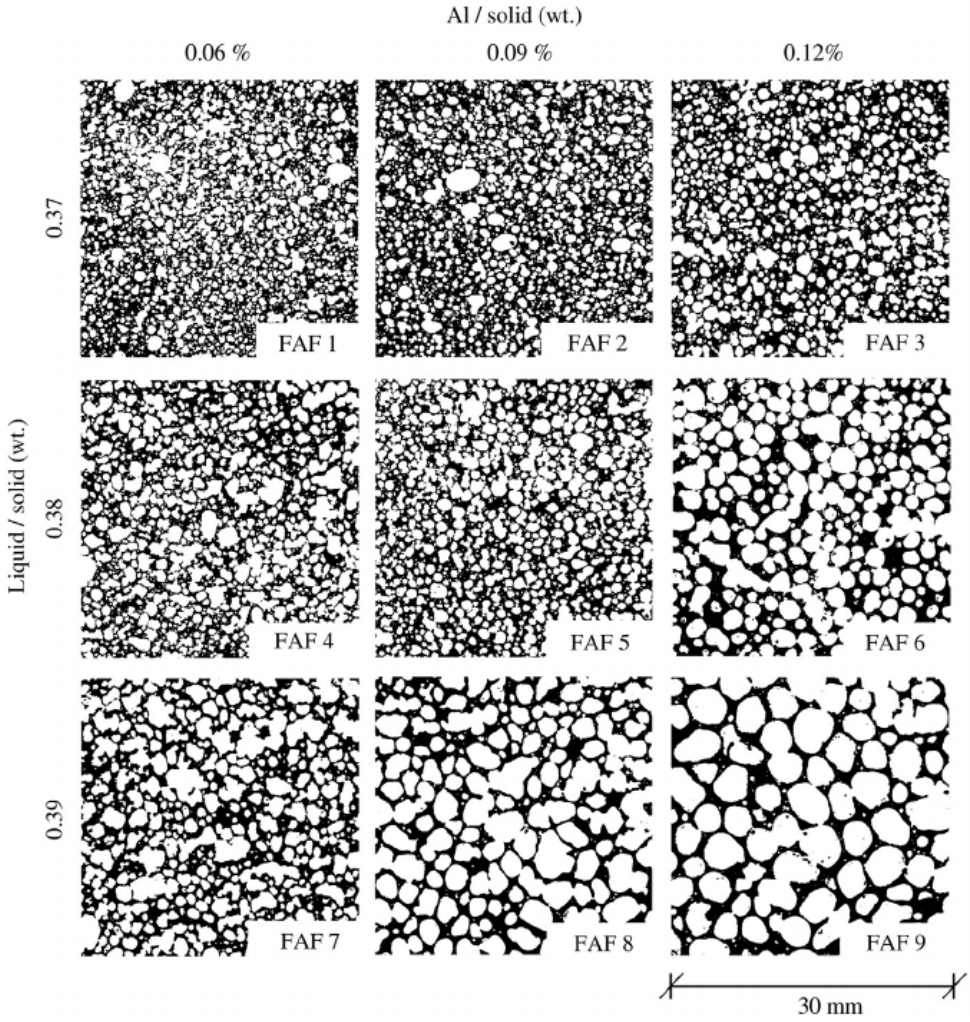

Figure 14: Polished sections of the foams[16]

Further tests were carried out on a FAF 5 specimen as the most characteristic one.

Fire resistance of foams

Fire resistance tests used heating rate 3°C/min, two hours duration at maximum temperature and cooling rate -1°C/min[16]. Figure 15 shows the change of volume, mass, and colour of FAF 5 after the fire-resistance test. Almost all chemically and physically bound water is removed already at 800°C. The highest shrinkage increment appears between 800°C and 1100°C which is related to gel sintering. The sintering leads to embodying Na directly in glass, implying a loss of efflorescence. The compressive strength 5.99 MPa of the reference sample rose up to 13.25 MPa at 1100°C.

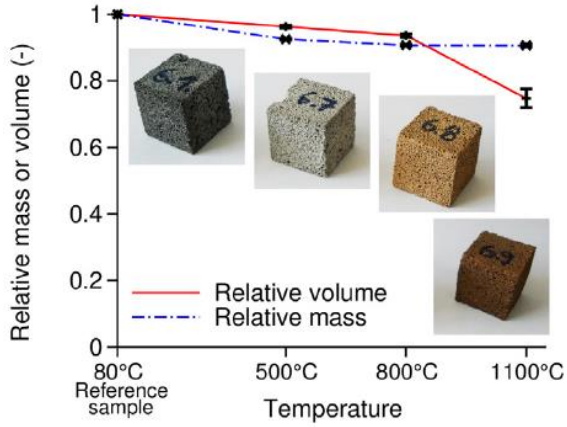

Figure 15: Relative changes of mass and volume during fire resistance test

Chemical resistance of foams

Chemical resistance was tested by a long-term immersion into excessive aggressive solutions, *i.e.* Na_2SO_4 44 g/l, $MgSO_4$ 5 g/l, NaCl 164 g/l, H_2SO_4 pH 2, HCl pH 2. It is evident that acids cause the most severe degradation by two mechanisms simultaneously. The first corresponds to Al depletion from N-A-S-H gel; specifically, the leaching leads to the ejection of Al from the aluminosilicate framework, leaving a relatively strong Si–O–Si skeleton, whereas the second mechanism corresponds to the dissolution of N-A-S-H gel in a low pH environment.

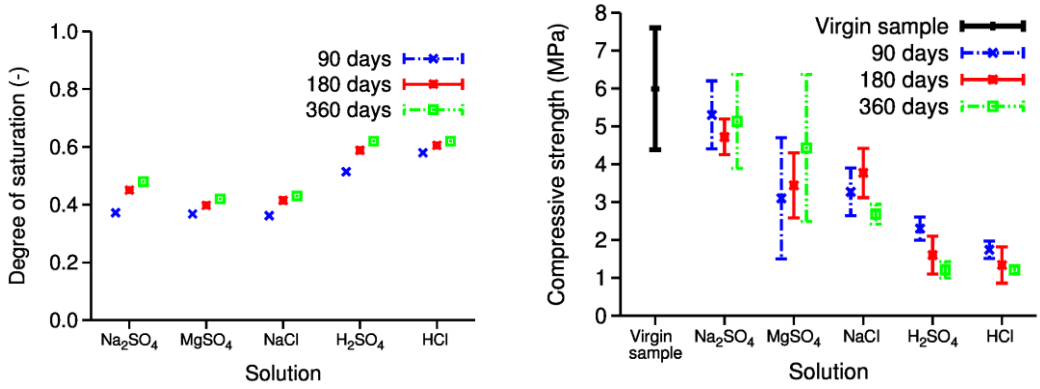

Figure 16: Degree of saturation and compressive strength in aggressive environments

Macroscopic elastic modulus of foams

Effective Young's modulus provides useful information on the microstructure, especially the interconnectedness of phases and their intrinsic elastic properties. A 2D scan of FAF 5 in Figure 14 served as a starting image for thresholding. A burning algorithm explored the paste connectedness within the images. As the macroporosity increases, several unconnected paste clusters emerged. Solid percolation threshold represents the macroporosity where no path between the top and the bottom exists. In our particular case, this corresponds to a macroporosity of 0.72, which equals to the foam bulk density of 490 kg/m^3. This result is in agreement with the lowest bulk density achieved 400 kg/m^3 in our experiments.

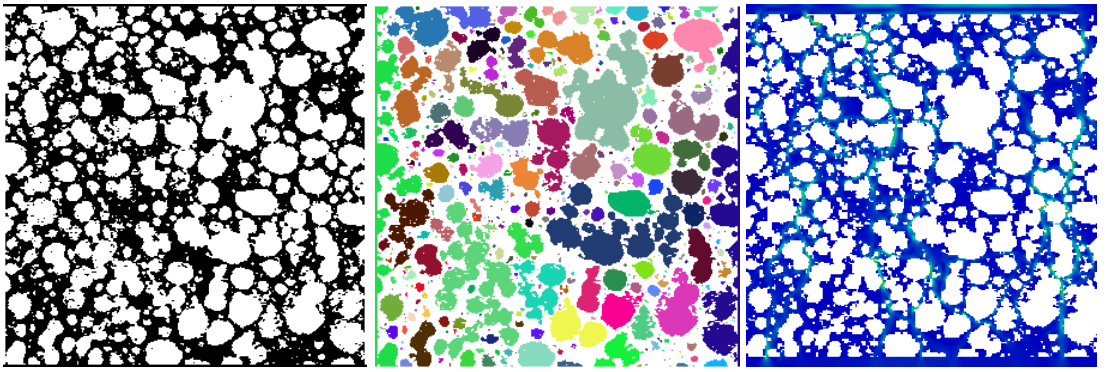

Figure 17: Image processing from black/white segmentation, pore connectedness and stress trajectory

Quadrilateral finite elements with linear approximations meshed a 2D microstructure by 500 × 500 elements with an element size of 40 µm. The horizontal edges are loaded by kinematic uniform boundary conditions in the form of a prescribed displacement, while the vertical edges are kept free. The intrinsic Young's modulus of alkali-activated paste is of 35.35 GPa and the Poisson's ratio is set at 0.2.

Macroscopic Young's modulus is showed in Figure 18 for varying macroporosity and agrees well with experimentally measured values.

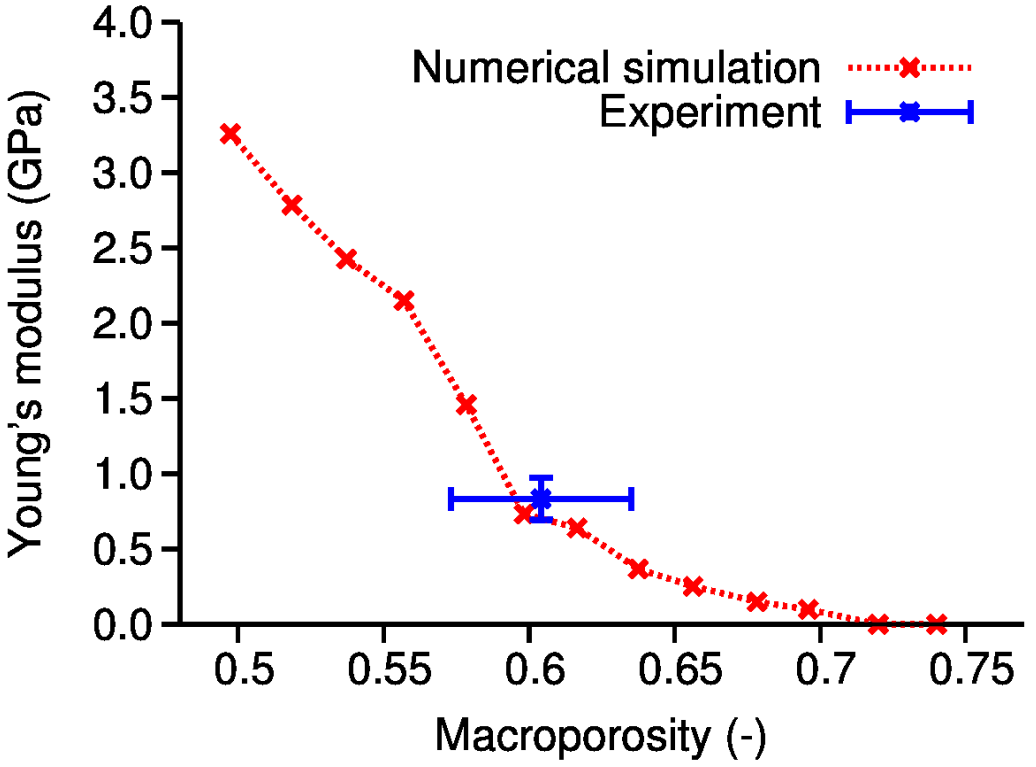

Figure 18: Young's modulus for various macroporosities

Conclusions

Microstructures of materials can be engineered with the help of multiscale simulation tools. While elastic predictions are generally well elaborated for composite materials, strength predictions remain a challenging task due to strain localisation, statistical nature of underlying microstructures, interfaces and spatial gradients.

Slag as a supplementary cementitious material brings the advantage of additional C-S-H formation during hydration and thus promotes a long-term strength. Slag can act as a centre for nucleation sites and enhance more homogeneous C-S-H distribution leading especially to a higher short-term strength.

Alkali-activated fly ash foams have excellent properties in chemical durability and fire resistance. Slag could be incorporated to the foams as well, bringing a beneficial increase of early-age strength.

We gratefully acknowledge financial support from Competence Centres program of Technology Agency of the Czech Republic (TA CR) under the project Centre for Effective and Sustainable Transport Infrastructure TE01020168.

References

1. J. T. Oden, K. Vemaganti and N. Moës, “Hierarchical modeling of heterogeneous solids”, *Comput Method Appl M*, **172** (1-4) 3-25 (1999).
2. T. C. Powers and T. L. Brownyard, “Studies of physical properties of hardened portland cement paste”, *Bulletin 22*, Research Laboratories of the Portland Cement Association, Chicago, 1948.
3. P. Termkhajornkit, Q. H. Vu, R. Barbarulo, S. Daronnat and G. Chanvillard, “Dependence of compressive strength on phase assemblage in cement pastes: Beyond gel–space ratio — Experimental evidence and micromechanical modelling”, *Cem Concr Res*, **56** (0) 1–11 (2014).
4. Database CemBase, version 2016-10-20. Downloadable from http://mech.fsv.cvut.cz/~smilauer.
5. P. E. Roelstra, H. Sadouki and F. H. Wittmann, “Le béton numérique”, *Mater Struct*, **18** 327-335 (1985).
6. O. Bernard, F.-J. Ulm and E. Lemarchand, “A multiscale micromechanics-hydration model for the early-age elastic properties of cement-based materials”, *Cem Concr Res*, **33** (9) 1293-1309 (2003).
7. B. Pichler and C. Hellmich, “Upscaling quasi-brittle strength of cement paste and mortar: A multi-scale engineering mechanics model”, *Cem Concr Res*, **41** (5) 467-476 (2011).
8. G. Cusatis, Z. P. Bažant and L. Cedolin, “Confinement-shear lattice model for concrete damage in tension and compression: II. Computation and validation”, *J Eng Mech*, **129** (12) 1449–1458 (2003).
9. P. Grassl and M. Jirásek, “Meso-scale approach to modelling the fracture process zone of concrete subjected to uniaxial tension”, *Int J Solids Struct*, **47** (7–8) 957–968 (2010).
10. A. Griffith, Theory of rupture, in: C. Biezeno, J. Burgers (Eds.), *First International Congress for Applied Mechanics*, Delft, 55-63 (1924).
11. M. Hlobil, V. Šmilauer and G. Chanvillard, “Micromechanical multiscale fracture model for compressive strength of blended cement pastes”, *Cem Concr Res*, **83** (0) 188-202 (2016).
12. M. Vořechovský, “Interplay of size effects in concrete specimens under tension studied *via* computational stochastic fracture mechanics”, *Int J Solids Struct*, **44** 2715–2731 (2007).
13. A. O. Purdon, “The action of alkalis on blast-furnace slag”, *J Soc Chem Ind Trans Commun*, **59** 191-202 (1940).
14. C. Shi, D. Roy and P. Krivenko, “Alkali-Activated Cements and Concretes”, Taylor & Francis, 2005.
15. V. Šmilauer, P. Hlaváček, F. Škvára, R. Šulc, L. Kopecký and J. Němeček, “Micromechanical multiscale model for alkali activation of fly ash and metakaolin”, *J Mat Sci*, **46** (20) 6545-6555 (2011).
16. P. Hlaváček, V. Šmilauer, F. Škvára, R. Šulc and L. Kopecký, “Inorganic foams made from alkali-activated fly ash: Mechanical, chemical and physical properties”, *J Eur Ceram Soc*, **35** (2) 703-709 (2015).
17. J. Němeček, V. Králík, V. Šmilauer, L. Polívka and A. Jäger, “Tensile strength of hydrated cement paste phases assessed by microbending tests and nanoindentation”, *Cem Concr Comp*, **73** 164-173 (2016).